

Article

RETRACTED: Impact of High-Frequency Traveling-Wave Magnetic Fields on Low-Conductivity Liquids: Investigation and Potential Applications in the Chemical Industry

Xinyu Cui ^{1,2}, Xianzhao Na ^{1,*}, Xiaodong Wang ^{2,*}, Roland Ernst ³ and Fautrelle Yves ³

¹ State Key Laboratory of Advanced Steel Processing and Products, Central Iron and Steel Research Institute, Beijing 100081, China; cuixinyu0626@163.com

² College of Material Science and Opto-Electronic Technology, University of the Chinese Academy of Sciences, Beijing 100049, China

³ Université Grenoble Alpes, CNRS, Grenoble INP, SIMAP, F-38000 Grenoble, France

* Correspondence: na_cisri@126.com (X.N.); xiaodong.wang@ucas.ac.cn (X.W.)

Abstract: High-frequency traveling-wave magnetic fields refer to alternating magnetic fields that propagate through space in a wave-like manner at high frequencies. These magnetic fields are characterized by their ability to generate driving forces and induce currents in conductive materials, such as liquids or metals. This article investigates the application and approaches of a unique form of high-frequency traveling-wave magnetic fields to low-conductivity liquids with conductivity ranging from 1 to 102 S/m. Experiments were conducted using four representative electrolytic solutions commonly employed in the chemical industry: sulfuric acid (H₂SO₄), sodium hydroxide (NaOH), sodium chloride (NaCl), and ionic liquid ([Bmim]BF₄). The investigation focuses on the impact of high-frequency magnetic fields on these solutions at the optimal operating point of the system, considering the effects of Joule heating. The findings reveal that the high-frequency traveling magnetic field exerts a significant volumetric force on all four low-conductivity liquids. This technology, characterized by its non-contact and pollution-free nature, high efficiency, large driving volume, and rapid driving speeds (up to several centimeters per second), also provides uniform velocity distribution and notable thermal effects. It holds considerable promise for applications in the chemical industry, metallurgy, and other sectors where enhanced three-phase transfer processes are essential.



Citation: Cui, X.; Na, X.; Wang, X.; Ernst, R.; Yves, F. RETRACTED: Impact of High-Frequency Traveling-Wave Magnetic Fields on Low-Conductivity Liquids: Investigation and Potential Applications in the Chemical Industry. *Materials* **2024**, *17*, 944. <https://doi.org/10.3390/ma17040944>

Academic Editors: Natalia I. Tsyntaru and Henrikas Cesiulis

Received: 14 January 2024
Revised: 5 February 2024
Accepted: 7 February 2024
Published: 18 February 2024
Retracted: 30 October 2024



Copyright: © 2024 by the authors. Licensee MDPI, Basel, Switzerland. This article is an open access article distributed under the terms and conditions of the Creative Commons Attribution (CC BY) license (<https://creativecommons.org/licenses/by/4.0/>).

Keywords: electromagnetic drive; high-frequency traveling magnetic field; low electrical conductivity; ionic liquid

1. Introduction

Electromagnetic drive technology plays a critical role in the electromagnetic processing of materials and can be broadly categorized into electromagnetic stirring and electromagnetic pumps [1]. In metallurgy, electromagnetic stirring utilizes the Lorentz force to agitate high-temperature metal liquids in continuous-casting billets that have not solidified. This contactless method enhances the convection of the metal liquid, controlling the solidification process and ensuring a high-quality output. On the other hand, electromagnetic pumps, employed in industries such as chemical, atomic energy, and metallurgical foundries, generate a directional flow of liquid metal through the interaction between magnetic fields and electric currents. Sulfuric acid, sodium hydroxide, and sodium chloride solutions represent acidic, alkaline, and neutral electrolyte systems commonly employed across industries such as metallurgy, chemical engineering, and food processing. Their experimental investigation provides useful insights into driving low-conductivity liquids with varying physicochemical properties.

This technology is indispensable for the transportation of hazardous heavy metals (e.g., mercury, liquid lead, and their alloys) and chemically active metals (e.g., potassium,

sodium, and their alloys) as well as high-temperature metal liquids. Currently, electromagnetic drive technology is predominantly applied to liquids with a high conductivity (10^5 – 10^7 S/m). However, there exists significant potential for its application in low-conductivity liquids (1 – 10^2 S/m), which the existing technology, typically operating below 100 Hz [2], struggles to effectively drive due to the limited generation of Lorentz force under these conditions. High-frequency magnetic fields in industry are mainly harnessed for their thermal effects, such as in high-frequency induction heating, and are not commonly used for electromagnetic drive due to the skinning effect. To drive a low-conductivity liquid through electromagnetic technology, the effectiveness of the electromagnetic drive can be assessed through the skinning depth δ , as outlined in Equation (1):

$$\delta = \sqrt{\frac{1}{\pi f \mu_0 \sigma}} \quad (1)$$

where f is the frequency of the input current, μ_0 is the vacuum permeability, and σ is the conductivity of the liquid. Optimal magnetic field penetration occurs when the skinning depth is between 0.2 and 0.5 times the container's diameter. Contrary to traditional applications, this necessitates a high-frequency operating current to drive low-conductivity liquids effectively. Inspired by single-phase asynchronous motors, Ernst et al. [3] innovated a high-frequency electromagnetic drive capable of operating above 100 kHz. This technology successfully propelled a saturated NaCl solution (conductivity of 40 S/m) at centimeter-per-second speeds, demonstrating its potential for low-conductivity liquids. Subsequent research, including the work of Xiaodong et al. [4] and Li Yong [5], further validated this approach through theoretical analysis and experimental design. Wang et al. developed a numerical model of electromagnetism, enhancing our understanding of the high-frequency traveling magnetic field's principles, while Li Yong focused on optimizing the circuit-operating point by analyzing coil distances. Additionally, Guo et al. [6] examined the effects of various electrical parameters and coil configurations on the flow and temperature fields of low-conductivity liquids, contributing to the optimization of this technology. However, previous studies primarily tested simple media like NaCl solutions and lacked a comprehensive exploration of the driving effect on diverse electrically conductive solutions from an industrial perspective. This paper addresses this gap by using a high-frequency traveling-wave magnetic field to drive various low-conductivity industrial liquids, including H_2SO_4 , NaOH, NaCl solutions, and the ionic liquid [Bmim]BF₄. By employing particle image velocimetry (PIV), we quantitatively and dynamically measured the flow fields, comparing the driving effects on different media and analyzing the thermal effects produced. This study demonstrates the potential of high-frequency traveling magnetic field technology for industrial applications.

High-frequency traveling-wave magnetic field drive technology offers significant advantages, including non-contact operation, pollution-free processes, and high efficiency. Capable of propelling low-conductivity liquids at speeds of centimeters per second in large containers, it also imparts a measurable thermal effect. This technology finds diverse applications in various industries. In iron and steel metallurgy, for instance, where liquid steel slag typically has a conductivity of around 100 S/m [4], the conventional iron recovery process involves screening, crushing, and magnetic separation. This method is energy-intensive and generates substantial amounts of dust. Employing high-frequency traveling-wave magnetic field technology for separating liquid steel and slag can not only reduce pollution but also simplify the process.

In non-ferrous metallurgy, the pressurized leaching method is often used for low-grade ore processing, applicable to metals like copper, zinc, nickel, cobalt, tungsten, and various rare metals [5]. This method involves submerging the ore in acidic solutions for pressurization, heating, and stirring. Traditional mechanical stirring in pressurized leaching kettles often leads to poor sealing, risking hazardous liquid leakage and corrosion by acidic solutions [6]. High-frequency traveling-wave magnetic field technology can overcome

these challenges by providing non-contact stirring and heating, enhancing uniformity and reducing equipment failure. The chemical industry frequently employs the hydrothermal method for inorganic synthesis and material processing, such as in the production of nanopowders or thin films [7]. In traditional methods, the utilization of concentrated acids or alkalis in industrial processes necessitates the use of equipment capable of withstanding high temperatures, pressures, and corrosive environments. However, achieving adequate stirring under these conditions poses a challenge, making large-scale reactor production technically intricate and costly [8–11]. To address these issues, high-frequency traveling-wave magnetic field drive technology offers a solution by enabling non-contact stirring and heating of the electrolyte within enclosed reactors. Ionic liquids, which are organic salts with melting points below 100 °C, are commonly employed in solid–liquid stirring systems within the chemical industry due to their favorable electrical conductivity and thermal stability. For instance, [Bmim]BF₄ exhibits a conductivity of up to 4.7 S/m. The conventional mechanical stirring method often results in uneven flow fields and stagnant areas. Electromagnetic drive technology has the potential to revolutionize this process by utilizing Lorentz forces to uniformly and efficiently stir the entire conductive liquid [8].

This article shows a detailed experimental study of the high-frequency traveling-wave magnetic field drive device proposed by R. Ernst et al. [3]. The experiments utilized four different solutions—H₂SO₄, NaOH, NaCl, and the ionic liquid [Bmim]BF₄—each representing distinct industrial applications. The objective of this study was to explore the driving effect of the high-frequency traveling-wave magnetic field on these solutions and analyze its influences of conductivity.

2. Experimental Setup and Test System

In this study, R. Ernst et al. [3] designed a magnetic traveling field stirring installation. The setup comprises a high-frequency generator, a pair of capacitors, two-phase inductive coils, and cylindrical containers filled with electrolyte. A schematic diagram of this installation is presented in Figure 1.

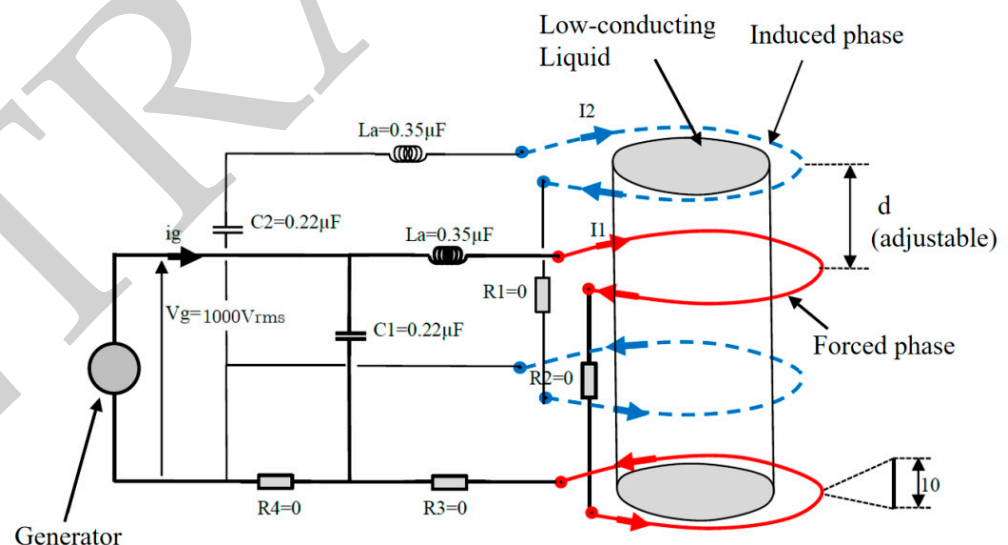


Figure 1. Simplified schematic of double-phase magnetic traveling field stirring installation [3].

The low-conductivity liquids tested in this experiment included aqueous solutions of 30% mass fraction sulfuric acid (H₂SO₄), 20% mass fraction sodium hydroxide (NaOH), saturated sodium chloride (NaCl), and an aqueous solution of 2.5 mol/L ionic liquid ([Bmim]BF₄).

The high-frequency generator used in this study is the CELES MP25kW GRI 25/4, manufactured by Five Celes, France. It operates based on the principle illustrated in Figure 1, generating a high-frequency current through an internal MOS transistor generator.

This generator features an output frequency range of 100 to 400 kHz and a power output of 25 kW. Its display terminal shows the real-time output current and voltage, frequency, power, and other system states, also enabling control over power output percentage. The accompanying capacitors, also from Five Celes, are of the ALU CU model with a capacitance of 0.21 μF . As shown in Figures 2 and 3, the two-phase inductor coils consist of a drive phase and an induction phase. These high-frequency inductor coils, made from 10 mm diameter copper tubing in a reverse-winding configuration, incorporate internal cooling water and are configured into helical coils with a 320 mm diameter. The neighboring coils of the same phase have currents flowing in opposite directions. The system involves a mutual inductance circuit composed of two-phase coils connected in parallel to the capacitor box. A drive-phase coil, connected to a high-frequency generator, generates an alternating magnetic field, while an induction-phase coil induces a high-frequency current. The specified capacitance of the capacitor box ensures an appropriate phase difference between the two-phase coils, resulting in the creation of an axial traveling magnetic field within the coil space. The direction of the magnetic field relies on the phase difference between the currents in the two-phase coils, with an upward-moving traveling-wave magnetic field occurring when the induction phase current lags behind the drive phase, and vice versa. The mutual inductance value can be adjusted by changing the spacing between the two-phase coils, thereby modifying the amplitude ratio and phase difference of the currents. This, in turn, alters the spatial distribution and motion pattern of the traveling-wave magnetic field. Inside the coil, an acrylic drum with dimensions of 390 mm in height and 290 mm in inner diameter is positioned, maintaining an 11 mm gap between the inner wall of the drum and the coil. The low-conductivity liquids tested in this experiment included H_2SO_4 , NaOH, NaCl solutions, and an ionic liquid solution ($[\text{Bmim}]\text{BF}_4$), representing acidic, alkaline, neutral, and organic solution systems in the chemical industry, respectively. Table 1 presents the relevant physical parameters of these liquids. While their densities and viscosities are similar, their conductivities vary significantly. Prior to driving each liquid, determining the system's optimal operating point is essential [5]. This point depends solely on the mutual and self-inductance of the drive and induction phases. Since the self-inductance coefficient of the coil is fixed post winding, and the capacitance value of the capacitor box is also set, adjusting the spacing between the two-phase coils is the only way to achieve the optimal working point. Within the inductance adjustment range of the driving phase, increasing the distance between the two-phase inductors elevates circuit impedance. Hence, adjusting this distance enables impedance matching between the high-frequency generator and the load, optimizing the generator's output power. In this experiment, a two-dimensional PIV system was employed, using a 5 MP high-speed camera capturing images at 200 fps with an exposure time of 300 μs and a resolution of 932×864 pixels. Hollow glass beads averaging 50 μm in diameter were used as tracers. The laser sheet was generated by a 5 W diode laser positioned 600 mm above the container, and the camera was laterally situated 1000 mm from the vessel center to capture a 27.5×25.5 cm field of view in the meridional plane.

Table 1. Main physical parameters of the low-conductivity liquid to be driven in this experiment.

	Conductivity 25 °C, S/m	Intensity g/cm^3	Concentration cP
H_2SO_4 (30%)	82.5	1.22	1.4
NaOH (20%)	40.0	1.21	1.8
NaCl (saturated)	23.1	1.33	1.9
$[\text{Bmim}]\text{BF}_4$ (2.5 mol/L)	4.7	1.08	1.5

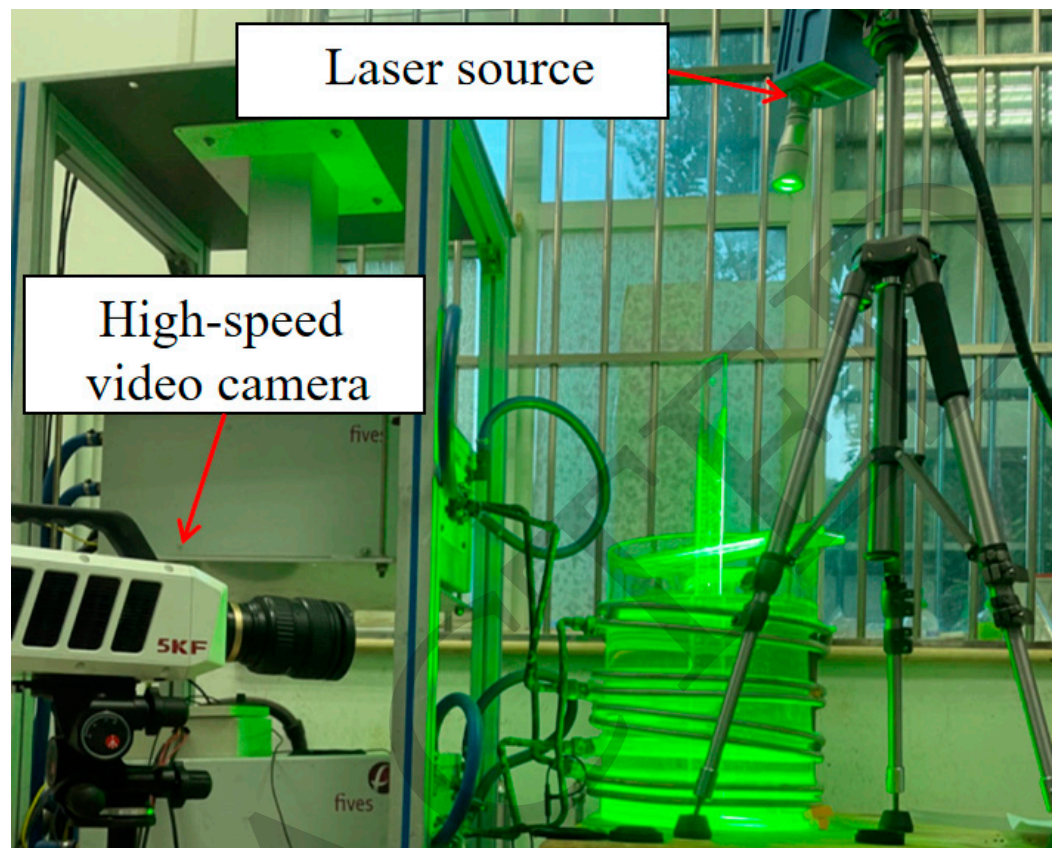


Figure 2. Schematics of the PIV system.

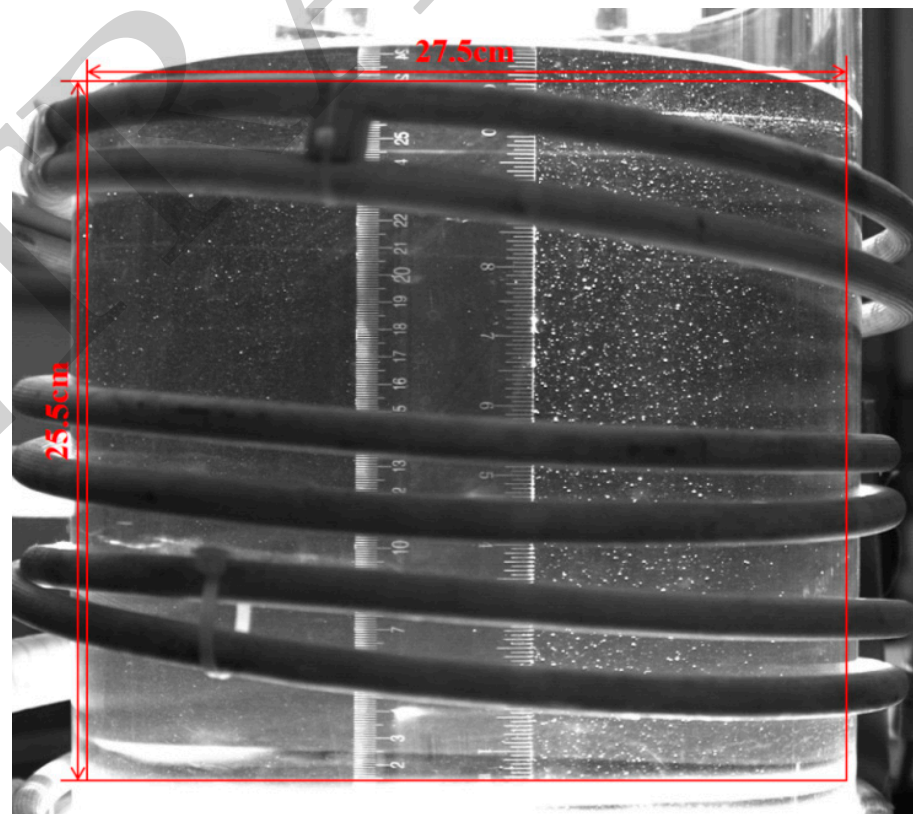


Figure 3. Placement of coils around weakly conductive fluid containers and filming locations.

The output parameters of the high-frequency (HF) power supply, including current, voltage, frequency, and power, can be ascertained by reading the display screen on the power supply cabinet. Additionally, the phase difference and amplitude ratio of the currents in the two-phase coils are measured using two Roche coils (CWT mini HF 30R). In this research, a two-dimensional particle image velocimetry (PIV) system was employed to measure the flow field distribution of a liquid within the meridional plane of a cylindrical vessel. To minimize laser shielding by the coil and maximize the field of view, the laser sheet light source (SM-SEM1-10W) was positioned above the vessel. This setup aligned the vertical laser plane with the vessel's center plane, while a high-speed camera (5KF10) was situated laterally to capture the flow field in this central plane, as illustrated in Figure 2. Hollow glass beads, averaging 50 μm in diameter, served as particle tracers. The high-speed camera recorded at 200 frames per second with an exposure time of 300 μs , producing images with a resolution of 930×860 pixels. For image analysis, the open-source Matlab-based software PIVlab (GUI. Version 2.63.0.) was utilized. This involved setting a query window of 32×32 pixels to analyze pairs of adjacent images via a mutual correlation algorithm (FFT). The process of filtering, correcting, and smoothing the data led to the derivation of velocity vector fields and velocity intensity gradient cloud maps within the interrogation windows. Post-processing utilizing vector validation and smoothing functions derived the final flow characterization results.

3. Operating Parameters of the System

For each low-conductivity liquid drive, the distance between the drive-phase and induction-phase coils was adjusted, thereby altering the mutual inductance between the two. This adjustment facilitated impedance matching between the high-frequency generator and the load, optimizing the power supply's output to its maximum. At this optimal operating point, the phase difference between the two-phase coils approached 90° , ensuring the most effective driving action of the high-frequency traveling-wave magnetic field. The optimal operating parameters for different media are presented in Table 2.

Table 2. Electrical parameters of the optimal operating point of the system when driving different media.

	Conductivity σ 25 °C, S/m	Frequency f kHz	Power P kW	Phase Difference φ °	Skin Depth δ m
H ₂ SO ₄ (30%)	82.5	238	24.3	109	0.11
NaOH (20%)	40.0	248	17.0	62.3	0.16
NaCl (saturated)	23.1	254	13.1	40.6	0.21
[Bmim]BF ₄ (2.5 mol/L)	4.7	262	6.8	33.2	0.45

Skin depth (δ) refers to the penetration depth of an electromagnetic field into a conductor, which is inversely proportional to the square root of conductivity, frequency, and permeability. As indicated by the table, the conductivity of the driving medium significantly influences the system's operating parameters. This is due to the interplay between the output power of the high-frequency generator and the external circuit's impedance. Changes in the conductivity of the low-conductivity liquid result in corresponding changes in the external circuit's impedance, dynamically affecting the power supply's output power and the phase difference in the two-phase coil. In optimal operating conditions, a higher conductivity of the driven liquid correlates with an increased power supply output and a phase difference in the two-phase coil closer to 90° . The table also reveals that a lower conductivity in the driving liquid necessitates a higher output frequency from the generator. This is because the impedance characteristics of the two-phase inductive system and the resonance frequency of the two-phase coil current vary with the conductivity of the driving solution. Consequently, the high-frequency generator must operate at the resonance point of the parallel connection, necessitating an adjustment in the output frequency. The relationship between operating parameters and conductivity in Table 2 can be mathematically expressed using Ohm's law. According to Ohm's law, conductivity plays a crucial role

in determining impedance, which, in turn, affects the current induced and the driving force generated for a specific voltage input. A higher conductivity value leads to lower impedance and stronger driving effects.

4. Flow Field Analysis

Given the motion pattern of the high-frequency traveling-wave magnetic field, the coil winding method, and the properties of the driven cylindrical liquid, it is clear that the driving solution must generate a three-dimensional flow.

The flow field in the meridional plane of the container, which is primarily influenced by the axial direction of the traveling-wave magnetic field and the Lorentz force, is subjected to a quantitative analysis. To effectively illustrate the driving effect of the high-frequency traveling-wave magnetic field, the flow field within this plane is photographed and examined. At the optimal working point specified in Table 2, the axial center plane's flow field is captured using a high-speed camera. Due to partial obstruction of the field of view by the coil and optical aberrations from the cylindrical container's curved edges, the analysis requires cropping areas with excessive aberrations and the laser reflection's highlighted area at the bottom. Consequently, a rectangular section with dimensions of 27.5×25.5 cm in the center plane is selected for flow field analysis, as depicted in Figure 3, with the coil masked out. One limitation of the current study is that the flow field analysis is conducted within a rectangular section of dimensions 27.5×25.5 cm, selected to minimize optical aberrations while encompassing a representative area. However, as this section size represents only a subset of the full experimental container, its proportions relative to the overall vessel dimensions may impact the generalizability of the conclusions drawn regarding the flow behavior. While the analyzed region aims to capture characteristic flow patterns, its dimensions could potentially influence the representativeness of the overall flow field. This limitation should be acknowledged. Optimization of the analysis section dimensions and techniques enabling whole-field visualization, such as advanced particle image velocimetry (PIV), may help validate the conclusions by further establishing the translatability of insights beyond the bounds of the measurement area. Dimensional refinement and full-field approaches in future work could strengthen the validity of flow characterization. Hollow glass beads, $50 \mu\text{m}$ in average diameter, are used as tracer particles in the solution. The camera captures images at 200 frames per second with an exposure time of $300 \mu\text{s}$, and these images are processed using PIVlab to analyze and calculate the flow field distribution of the driven liquid.

4.1. Analysis of Flow Patterns

Figure 4 illustrates the flow field of a 30% mass fraction H_2SO_4 solution in a container, captured 15 s after initiating the high-frequency power supply. As depicted in Figure 4a, upon activation of the power supply, the liquid demonstrates a rapid flow response, transitioning from a state of disordered thermal motion to gradual acceleration under an electromagnetic force. Within 5 s, directional movement tendencies emerge, with the solution's central part beginning to flow downward. Figure 4b shows that, under an electromagnetic driving force, the solution's flow rate increases, leading to forced convection. This results in a double-loop flow, where the upper part of the container's two measured solutions converges towards the center. As driving time progresses, the Joule heat generated near the container wall adjacent to the coil accumulates, raising the temperature and initiating thermal convection. This, combined with forced convection, forms a turbulent vortex, as illustrated in Figure 4c. At this stage, the average flow rate reaches 7.2 cm/s , with a maximum of 13 cm/s , significantly enhancing the solution's flow under the influence of the high-frequency traveling-wave magnetic field.

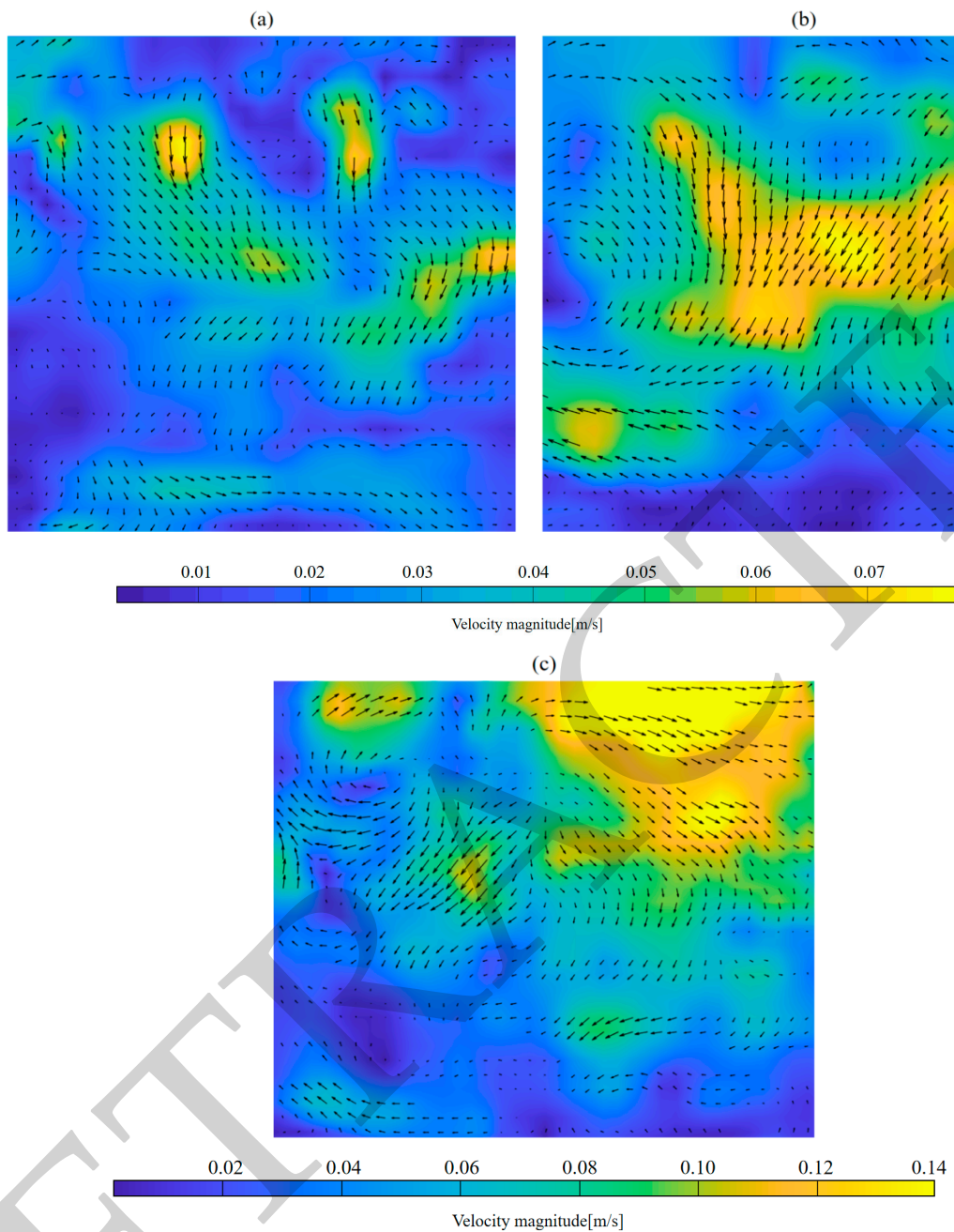


Figure 4. Velocity vectors and intensity distributions of the meridional flow field within 15 s after the startup of the high-frequency power supply: (a) $t = 5$ s, (b) $t = 10$ s, and (c) $t = 15$ s (the driving electrolytic solution is 30% H_2SO_4).

The solution's flow progression under the high-frequency traveling-wave magnetic field can be categorized into three phases: (1) acceleration from disordered thermal motion to directional motion; (2) a directional flow phase dominated by forced convection; and (3) a turbulent phase featuring a combination of thermal and forced convection. Figure 5 shows that, in the initial 0–6 s, the solution gradually accelerates to form an annular flow converging from both sides to the center due to the electromagnetic driving force. Between 6–12 s, the solution achieves the maximum forced convection velocity, with new vortices forming near the walls due to added thermal convection, further increasing the velocity. After 12 s, the velocity stabilizes, and the solution undergoes vigorous flow under the combined effects of electromagnetic and thermal buoyancy forces.

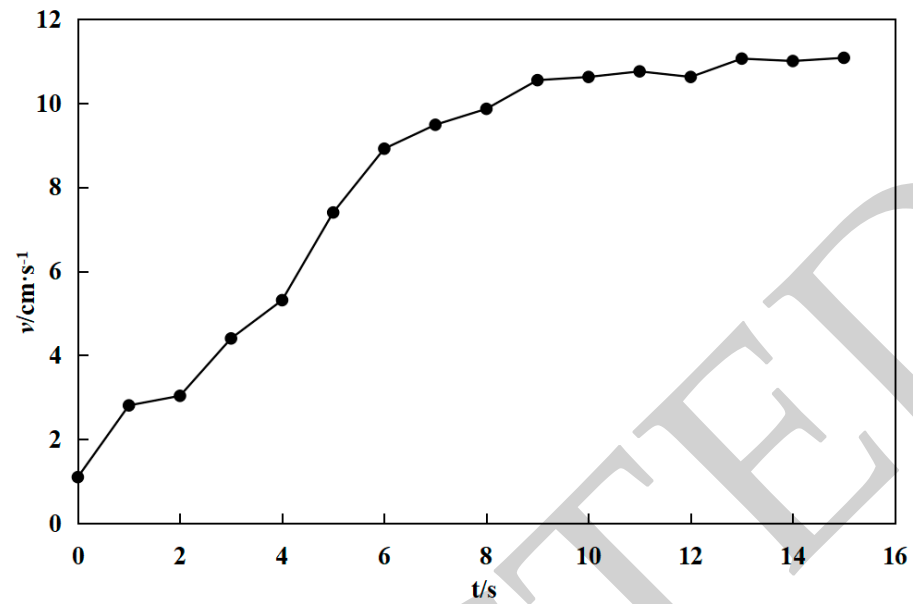


Figure 5. Maximum speed value versus time in 15s after startup of high-frequency power supply (the driving electrolytic solution is 30% H₂SO₄).

As shown in Figure 5, in order to investigate the driving effect of the high-frequency traveling magnetic field on the solutions at different locations in the container, we photographed the flow fields in the four regions from one to four within a short period of time, and, each time, the interval between the photographs was relatively short so that the effect of the temperature change due to Joule heat could be neglected. It can be seen that the average flow rate of the solution in the four regions is close, and the flow trend is consistent, as shown by the red trend line in the figure. They are all upward on both sides and downward in the center of the circulation, and the center part of the flow is stronger, but the regularity of the flow field in the local region is not obvious. Figure 6 shows the velocity gradient of region 2 when the maximum driving speed is reached, and it can be seen that the change in the flow velocity inside the whole fluid does not vary much, which also means that the high-frequency traveling magnetic field acts on the whole container, and there is no dead zone, which is significantly different from the mechanical stirring characteristics.

The momentum equation for the driving process is represented by Equations (2) and (3), which account for the thermal convection scenario and incorporate an electromagnetic force source term. In these equations, t denotes time, p represents pressure, ν is the kinetic viscosity, g signifies gravitational acceleration, β_0 is the coefficient of thermal expansion, ΔT indicates the temperature change, and F_{em} is the electromagnetic force source term. The driving process is influenced by the output power of the high-frequency power supply: a higher output power results in an increased coil current, thereby generating a stronger Lorentz force in the liquid and enhancing the driving speed. Concurrently, as the liquid's temperature rises, the role of thermal convection in influencing the liquid's flow also increases. The transition time between the different flow phases is dependent on the magnitude of the electromagnetic force and the thermal effect. Thus, liquids with a higher conductivity exhibit shorter transition times.

$$\rho \frac{Du}{Dt} + \rho(u \cdot \nabla)u = -\nabla p + \nu \nabla^2 u + F_{em} + \rho \beta_0 \Delta T g \quad (2)$$

$$\rho \nabla \cdot u = 0 \quad (3)$$

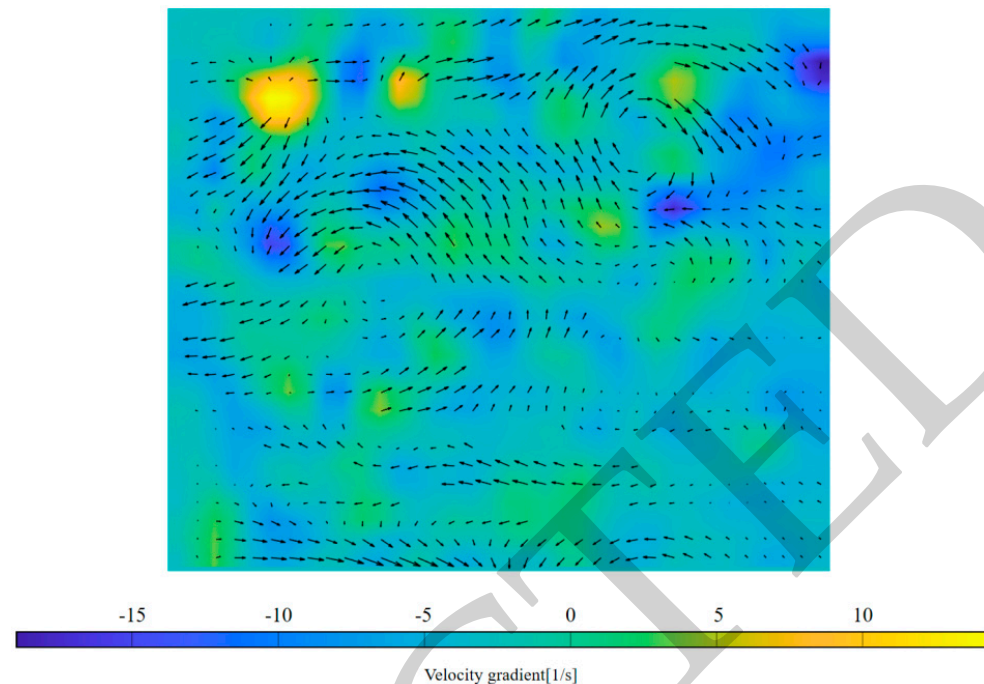


Figure 6. Velocity vector and velocity gradient distribution of the flow field (30% H₂SO₄).

The average flow rate of the solution is relatively uniform, exhibiting a coherent and consistent flow trend with upward movement on both sides and a downward circulation at the center, where the flow intensity is greater. Figure 6 presents the velocity gradient diagram at the point of maximum driving speed, indicating minimal change in the flow velocity throughout the fluid. This suggests that the high-frequency traveling-wave magnetic field influences the entire vessel uniformly, without creating any dead zones, a stark contrast to the characteristics of mechanical stirring. Furthermore, as inferred from both Figure 6 and Equation (2), since the Lorentz force acts as a non-contact volumetric force and the electromagnetic force source term in Equation (2) represents force density, the larger the fluid volume affected by the magnetic field, the greater the driving force. Consequently, the high-frequency traveling-wave magnetic field can uniformly drive low-conductivity fluids even in larger-sized containers. The homogeneous distribution of the high-frequency traveling-wave magnetic field throughout the container ensures that each component of the solution experiences a propelling force. This stands in contrast to traditional mechanical stirring methods, which, especially in the case of large containers, require careful consideration of factors such as the size and shape of the stirring paddle and are more susceptible to mechanical failures. Therefore, the implementation of high-frequency traveling-wave magnetic field drive technology offers significant advantages in various industrial applications.

4.2. Effect of High-Frequency Traveling-Wave Magnetic Field Direction on the Flow Field

During the operation of the high-frequency power supply, electrical energy is transformed into kinetic and thermal energy. In the solution, the induced current interacts with the high-frequency magnetic field to generate a driving force, while simultaneously producing Joule heat. Thus, the liquid's flow results from the combined effects of forced convection and thermal convection. In the solution, Joule heat-induced natural convection moves upward along the container walls, where the liquid near the wall is subjected to upward thermal buoyancy. In accordance with the principles of high-frequency traveling-wave magnetic field drive, the proximity to the coil amplifies magnetic induction, thereby generating stronger induced currents and more substantial Lorentz forces. The movement direction of the high-frequency magnetic field and, consequently, the direction of the driv-

ing force on the liquid are influenced by the phase of the currents in the two-phase coils. This can lead to an upward or downward movement of the high-frequency magnetic field.

As shown in Figure 7, in Figure 7A, the driving phase current's phase leads the induction phase current, resulting in an upward direction of the traveling-wave magnetic field and aligning the electromagnetic force with the direction of thermal convection. Conversely, in Figure 7B, where the driving phase current's phase lags behind the induction phase current, the traveling-wave magnetic field moves downward, opposing the direction of thermal convection. It is evident that changing the direction of the traveling-wave magnetic field can significantly alter the flow direction of the liquid, while the maximum driving speed remains relatively constant. Therefore, by modifying the direction of the traveling-wave magnetic field, it is possible to achieve directional driving of low-conductivity liquids in various directions, leading to more optimal driving outcomes.

4.3. The Driving Effects of Different Liquids

Figure 8 displays the flow field distribution of three other low-conductivity solutions used in this experiment, captured at room temperature when the maximum driving effect was achieved after starting the high-frequency power supply ($t = 200$ s). The maximum flow speeds calculated for the H_2SO_4 solution, the NaOH solution, the NaCl solution, and the $[\text{Bmim}]\text{BF}_4$ ionic liquid solution in this region were 13, 9, 6, and 3 cm/s, respectively. Comparing the flow fields of solutions with different conductivities, it is observed that all four liquids exhibit a similar flow pattern, with higher conductivity fluids demonstrating more pronounced driving effects. This is attributed to the electromagnetic driving force being directly correlated with the liquid's conductivity. Furthermore, the densities and viscosities of these solutions are relatively similar. A higher conductivity results in a greater electromagnetic force and more significant Joule heating during the driving process, leading to more pronounced thermal convection and increased driving speeds. Consequently, a direct positive relationship exists between the driving speed and conductivity, as exemplified in Figure 9. Remarkably, even for ionic liquid solutions with a conductivity as low as 4.7 S/m, an average directional driving effect of 2 cm/s can be achieved. To accommodate liquids with varying conductivities, adjustments such as modifying the spacing between coils or altering the capacitor and resistor configurations of the system can be made to enhance the output power of the high-frequency power supply, thereby augmenting the driving effect. The advantage of the high-frequency traveling-wave magnetic field is its uniform distribution throughout the entire container, ensuring that each portion of the solution experiences a propelling force. This presents a clear advantage over the mechanical stirring methods currently utilized in industrial applications involving ionic liquids.

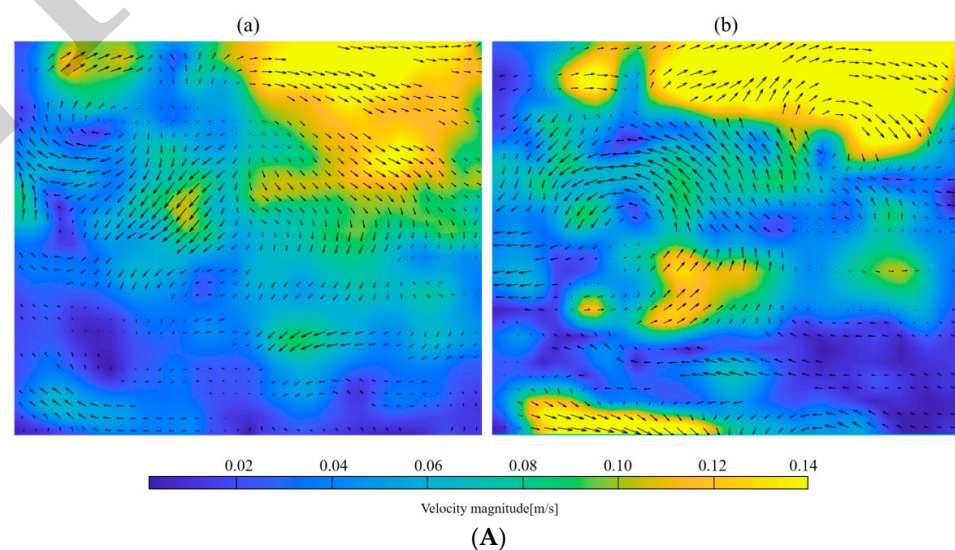


Figure 7. Cont.

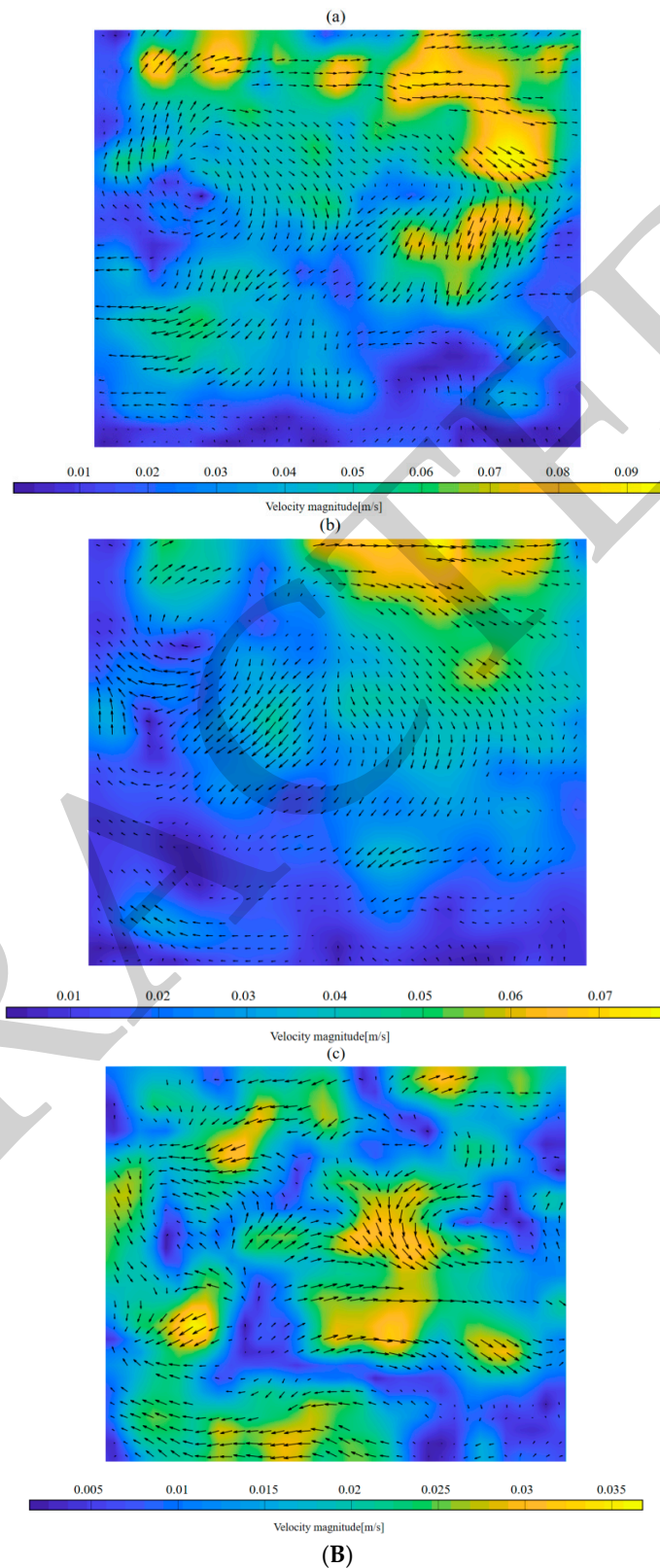


Figure 7. (A) Illustrates the driving effects of traveling-wave magnetic fields in different directions on low-conductivity liquids: (a) with the traveling-wave magnetic field oriented upwards, and (b) with the traveling-wave magnetic field oriented downwards (30% H₂SO₄). (B) Velocity vectors and intensity distributions of the flow field when driving different liquids: (a) NaOH (20%), (b) NaCl (saturated), and (c) [Bmim]BF₄ (2.5 mol/L).

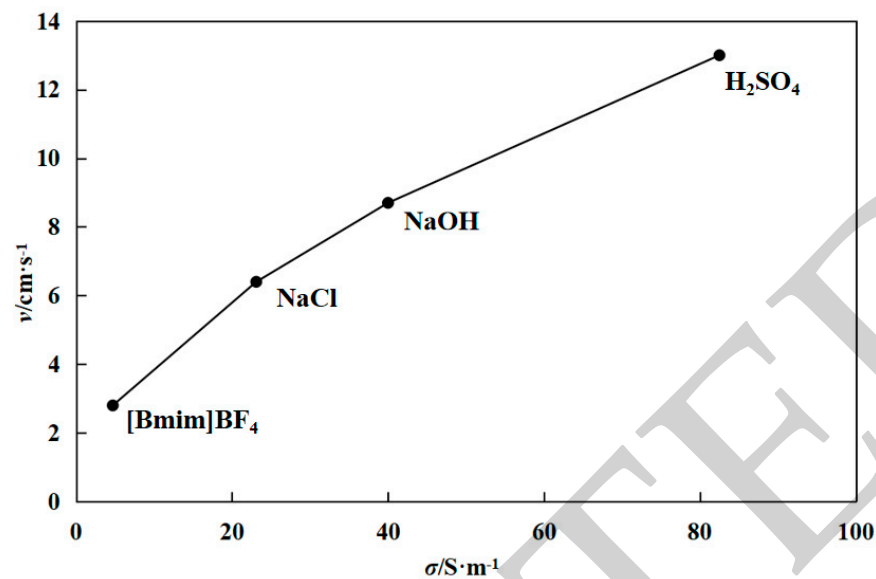


Figure 8. Maximum drive speed versus conductivity (the high-frequency generator was working at the optimal operating points in Table 2).

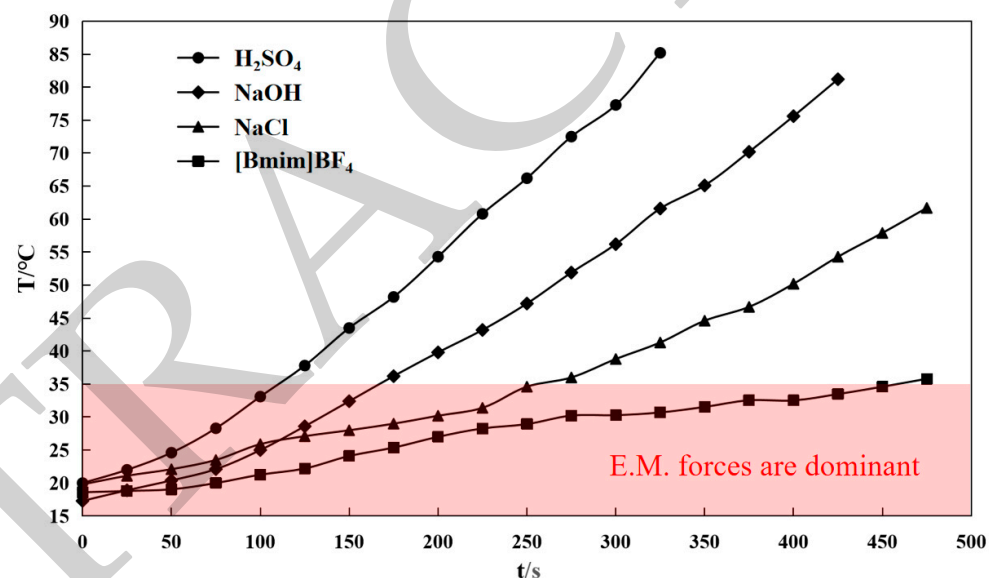


Figure 9. Warming curves of different media driven by high-frequency traveling-wave magnetic field.

Extensive research has been conducted across various industries, such as metallurgy, chemical engineering, and plasma processing, to study electromagnetic drive technology [12–14]. Its potential applications in improving convection and controlling solidification processes in high-temperature metal liquids through techniques like electromagnetic stirring and pumps have been investigated. The interaction between electromagnetic fields and different types of liquids, including ionic liquids and aqueous solutions, has also been examined [15–18]. Furthermore, the utilization of high-frequency magnetic fields, microwave, and ultrasonic processing has been explored for these methods' industrial applications. The generation and practical use of high-frequency electromagnetic waves, including the development of microwave sources, have been the subjects of thorough research [19–25]. The impact of magnetic fields on fluid flow and the challenges associated with generating millimeter-wave-to-terahertz and high-power microwaves have been extensively discussed. Additionally, the application of high-frequency electromagnetic fields in plasma processing, materials processing, and the electrical properties of foods has been investigated [26–32].

Despite these advancements, further research is necessary, particularly in exploring the potential of electromagnetic drive technology in low-conductivity liquids. Recent scientific investigations have studied a wide range of materials and their mechanical and chemical properties [33–37]. These studies include the manipulation of charge density in a solid–liquid triboelectric nanogenerator system, the development of sulfur-doped carbon-enhanced nanocomposites for sodium-ion storage, and the analysis of composite solid electrolytes for all-solid-state lithium metal batteries. Significant findings have been made in areas such as the controllable conductivity and ferromagnetism of secondary growth materials, the evaluation of hydrogen embrittlement behavior in stainless steel joints, and the measurement of residual stress in welding [38–42]. Many works' efforts have also focused on advancing high-entropy coatings with exceptional thermal protection properties, exploring metastable structures in superconducting films, and improving epoxy resin performance through the incorporation of boron nitride networks. Some research studies have developed the electrical resistivity–temperature characteristics of composite materials, developed efficient nanorod arrays for photoelectrochemical hydrogen evolution, and created flexible papers with superior electromagnetic interference shielding properties [43–47]. Considerations have also examined the sedimentation process in ferrofluids, utilized fluorophore molecules for dual-channel fluorescence chemo sensing, and employed MOFs as probes for water content measurement. Additionally, research has explored terahertz meta sensors for refractive index sensing and molecular identification, proposed linear free energy relationships for predicting partition coefficients in organic compounds, and studied the properties of conductive concrete mixed with nano graphite and magnetite sand [48–51].

5. Thermal Effect

While driving low-conductivity liquids, the application of a high-frequency traveling-wave magnetic field also induces a substantial thermal effect within the liquid. When the high-frequency power supply provides power to the liquid, a portion of electrical energy is converted into kinetic energy to propel the liquid, while another portion is transformed into Joule heat, gradually raising the temperature of the liquid. Figure 9 displays the temperature rise curves for the four different media measured using thermocouples, covering a period of 0–500 s at the optimal working point of the high-frequency traveling-wave magnetic field system (as specified in Table 2). The experiment was terminated when the temperature rise exceeded 80 °C. The results indicate that a higher conductivity of the driving liquid corresponds to a greater power output from the power source, resulting in more pronounced Joule heating and a faster temperature increase. As the liquid's temperature rises, its conductivity increases, causing changes in the load impedance of the high-frequency power source and consequently enhancing its output power. This correlation is also evident in Figure 9, where the heating rate of the various media accelerates with temperature. At lower temperatures, the electromagnetic driving force primarily influences the liquid's flow. However, as the driving time extends, the accumulated Joule heat gradually intensifies the thermal convection's impact on the liquid's flow, leading to irregular turbulent vortices. This is evident from the velocity vectors in Figure 7's flow field, where, after the same duration of power supply activation, the H₂SO₄ solution reaches the highest temperature, demonstrating the most noticeable irregular motion caused by thermal convection. In many industrial processes, such as the acid leaching process in non-ferrous metallurgy, chemical synthesis, and the high-temperature stirring of ionic liquids in catalytic processes, there is a need to simultaneously stir and heat low-conductivity liquids. In such scenarios, high-frequency traveling-wave magnetic field driving is particularly suitable.

In the context of future work, it is acknowledged that including data on the impact of varying concentrations would enhance the analysis. Regrettably, due to feasibility constraints, this study did not investigate concentration variations. However, it is an excellent suggestion for future research. From a qualitative perspective, it is anticipated

that there would be a positive correlation between the driving force and concentration up to a certain threshold, beyond which diminishing returns might occur. Collecting such data would provide valuable insights into this relationship. Magnetic fields are extensively utilized in diverse industrial sectors. They are employed in magnetic levitation systems to facilitate the operation of high-speed trains, employed in mining operations for magnetic separation processes, and employed in the field of medicine for magnetic resonance imaging (MRI), which enables non-invasive imaging of the human body [52–56]. Soft magnetic materials have gained significant attention due to their unique properties and potential applications in various fields. Their excellent magnetic characteristics, including high permeability and low coercivity, make them suitable for transformers, inductors, and magnetic storage devices [57–60]. The integration of soft magnetic materials into composites and their use in magnetic fluid hyperthermia have opened up new opportunities for research and development. This article explores the advancements in soft magnetic materials and their impact on composites and magnetic fluid hyperthermia and discusses their promising future prospects [60–62].

6. Conclusions

This paper presents a detailed experimental study of the high-frequency traveling-wave magnetic field drive device proposed by R. Ernst et al. The experiments utilized four different solutions— H_2SO_4 , NaOH, NaCl, and ionic liquid ($[\text{Bmim}]\text{BF}_4$)—each representing distinct industrial applications. This study explored the performance of the high-frequency power source in driving these different solutions, comparing the driving effects and thermal effects produced at the system's optimal working point. The experimental results show the following: The high-frequency traveling-wave magnetic field effectively drives all four low-conductivity liquids, achieving maximum driving speeds of 13, 9, 6, and 3 cm/s for the H_2SO_4 , NaOH, NaCl, and ionic liquid ($[\text{Bmim}]\text{BF}_4$) solutions, respectively. The driving force of the magnetic field acts uniformly throughout the container, without creating any dead zones. By altering the phase sequence of the current in the two-phase coils and consequently changing the direction of the traveling-wave magnetic field, the liquid's flow direction can be significantly changed without affecting the driving speed. The high-frequency traveling-wave magnetic field exhibits a notable thermal effect when driving low-conductivity liquids. At lower temperatures, the electromagnetic driving force dominates the liquid's flow. However, as the driving time increases, the accumulated Joule heat gradually intensifies the influence of thermal convection on the liquid's flow.

Higher conductivity of the driving liquid results in a greater power output from the source and a phase difference in the two-phase coils closer to 90° , enhancing both the driving effect and thermal impact. This correlation is related to the impedance characteristics of the dual-phase inductive system. Adjusting the spacing between the two-phase coils is necessary to achieve the system's optimal working point when driving liquids of different conductivities. Future research on driving liquids in containers of various sizes could involve adjustments to the circuit's capacitor values. This investigation utilizes high-frequency traveling magnetic field installations to conduct experiments on four commonly used low-conductivity liquids in the industry. The results of this study indicate that the implementation of high-frequency traveling magnetic field drive technology holds significant promise for various industrial applications. However, further research and exploration are required to assess its suitability in specific application scenarios. For example, in the metallurgical industry, where stirred slurry systems consist of solid–liquid two-phase media containing highly conductive metal blocks, future experiments should focus on employing high-frequency traveling magnetic field installations to drive such systems, specifically investigating the effects on low-conductivity liquids which contain metal particles or metallic liquids. Additionally, in the chemical industry, precise temperature control is crucial for many reactions. While the high-frequency traveling-wave magnetic field exhibits notable thermal effects when driving low-conductivity liquids, optimizing

the installation is essential to maintain effective driving while controlling the Joule heat generated by the liquid being processed.

Author Contributions: Methodology, X.C.; Software, X.N., X.W. and F.Y.; Validation, X.N., R.E. and F.Y.; Formal analysis, X.C., X.W., R.E. and F.Y.; Investigation, X.W. and F.Y.; Data curation, R.E. All authors have read and agreed to the published version of the manuscript.

Funding: This research received no external funding.

Data Availability Statement: Data are contained within the article.

Conflicts of Interest: The authors declare no conflict of interest.

References

- Asai, S. Birth and recent activities of electromagnetic processing of materials. *ISIJ Int.* **1989**, *29*, 981–992. [\[CrossRef\]](#)
- Yu, H.; Zhu, M. Numerical simulation of three-dimensional flow and temperature fields in electromagnetic stirring process of round billet crystallizer. *J. Met.* **2008**, *44*, 9.
- Ernst, R.; Perrier, D.; Brun, P.; Lacombe, J. Multiphase electromagnetic stirring of low conducting liquids. *COMPTEL-Int. J. Comput. Math. Electr. Electron. Eng.* **2005**, *24*, 334–343. [\[CrossRef\]](#)
- Wang, X.; Roland, E.; Yves, F. A Double-Phase high frequency Traveling Magnetic Field Developed for Contactless Stirring of Low-Conducting Liquid Materials. *CMES-Comput. Model. Eng. Sci.* **2021**, *127*, 469–489. [\[CrossRef\]](#)
- Li, Y. Study of High Frequency Traveling Wave Magnetic Field Enhanced Transport of Low Conductivity Liquids. Bachelor's Thesis, University of Chinese Academy of Sciences, Beijing, China, 2019.
- Guo, S.; Na, X.; Liu, R.; Li, Y.; Zhang, X.; Dong, H.; Dai, X.; Gong, X.; Wang, X. Numerical simulation of low conductivity liquid flow driven by high frequency traveling wave magnetic field. *J. Chin. Acad. Sci.* **2023**, *40*, 21–28.
- Mills, K.C.; Yuan, L.; Jones, R.T. Estimating the physical properties of slags. *J. S. Afr. Inst. Min. Metall.* **2011**, *111*, 649–658.
- Dai, Z.; Fang, J.; Zhao, A.; Yao, Z. Experimental study on copper leaching from a difficult-to-treat copper oxide ore with sulfuric acid. *Hydrometallurgy* **2018**, *37*, 4. [\[CrossRef\]](#)
- Zou, X.; Wang, H. An overview of pressurized reactor and its key ancillary equipment for nonferrous metal metallurgy. *Min. Metall.* **2016**, *25*, 60–64. [\[CrossRef\]](#)
- Hu, B.; Liu, J.T.; Chen, C.J.; Zhao, Z.; Chang, S.J.; Kang, P.L. Ultra-low charge transfer resistance carbons by one-pot hydrothermal method for glucose sensing. *Sci. China Mater.* **2017**, *60*, 1234–1244. [\[CrossRef\]](#)
- Moreno, M.; Castiglione, F.; Mele, A.; Pasqui, C.; Raos, G. Interaction of water with the model ionic liquid [Bmim][BF₄]: Molecular dynamics simulations and comparison with NMR data. *J. Phys. Chem. B* **2008**, *112*, 7826–7836. [\[CrossRef\]](#)
- Wang, P.; Cao, H.; Wang, F.; Zheng, Y.; Liu, R.; Dong, H.; Zhang, X.; Wang, X. Suspended particles behavior in aqueous [Bmim]BF₄ solution by novel on-line electrical sensing zone method. *Chem. Eng. Sci.* **2022**, *252*, 117280. [\[CrossRef\]](#)
- Garnier, M.; Moreau, R. Effect of finite conductivity on the inviscid stability of an interface submitted to a high-frequency magnetic field. *J. Fluid Mech.* **1983**, *127*, 365–377. [\[CrossRef\]](#)
- Leonelli, C.; Mason, T.J. Microwave and ultrasonic processing: Now a realistic option for industry. *Chem. Eng. Process. Process Intensif.* **2010**, *49*, 885–900. [\[CrossRef\]](#)
- Ives, R.L. Microfabrication of high-frequency vacuum electron devices. *IEEE Trans. Plasma Sci.* **2004**, *32*, 1277–1291. [\[CrossRef\]](#)
- Gilmour, A.S. *Klystrons, Traveling Wave Tubes, Magnetrons, Crossed-Field Amplifiers, and Gyrotrons*; Artech House: New York, NY, USA, 2011.
- Abdelsalam, S.I.; Vafai, K. Combined effects of magnetic field and rheological properties on the peristaltic flow of a compressible fluid in a microfluidic channel. *Eur. J. Mech.-B Fluids* **2017**, *65*, 398–411. [\[CrossRef\]](#)
- Booske, J.H. Plasma physics and related challenges of millimeter-wave-to-terahertz and high power microwave generation. *Phys. Plasmas* **2008**, *15*, 055502. [\[CrossRef\]](#)
- Borisevich, V.D.; Potanin, E.P. The concept of a plasma centrifuge with a high frequency rotating magnetic field and axial circulation. *Phys. Scr.* **2017**, *92*, 075601. [\[CrossRef\]](#)
- Kawamoto, H. Some techniques on electrostatic separation of particle size utilizing electrostatic traveling-wave field. *J. Electrostat.* **2008**, *66*, 220–228. [\[CrossRef\]](#)
- Liu, Y.X.; Zhang, Q.Z.; Zhao, K.; Zhang, Y.R.; Gao, F.; Song, Y.H.; Wang, Y.N. Fundamental study towards a better understanding of low pressure radio-frequency plasmas for industrial applications. *Chin. Phys. B* **2022**, *31*, 085202. [\[CrossRef\]](#)
- Conrads, H.; Schmidt, M. Plasma generation and plasma sources. *Plasma Sources Sci. Technol.* **2000**, *9*, 441. [\[CrossRef\]](#)
- Zhou, F.J.; Zhao, K.; Wen, D.Q.; Liu, J.K.; Liu, Y.X.; Wang, Y.N. Simulation of nonlinear standing wave excitation in very-high-frequency asymmetric capacitive discharges: Roles of radial plasma density profile and rf power. *Plasma Sources Sci. Technol.* **2021**, *30*, 125017. [\[CrossRef\]](#)
- Yang, Y.; Kushner, M.J. Modeling of dual frequency capacitively coupled plasma sources utilizing a full-wave Maxwell solver: I. Scaling with high frequency. *Plasma Sources Sci. Technol.* **2010**, *19*, 055011. [\[CrossRef\]](#)

25. Sansonnens, L.; Howling, A.A.; Hollenstein, C. Electromagnetic field nonuniformities in large area, high-frequency capacitive plasma reactors, including electrode asymmetry effects. *Plasma Sources Sci. Technol.* **2006**, *15*, 302. [[CrossRef](#)]
26. Kumar, N.; Singh, U.; Singh, T.P.; Sinha, A.K. A review on the applications of high power, high frequency microwave source: Gyrotron. *J. Fusion Energy* **2011**, *30*, 257–276. [[CrossRef](#)]
27. El Khaled, D.; Novas, N.; Gazquez, J.A.; Manzano-Agugliaro, F. Microwave dielectric heating: Applications on metals processing. *Renew. Sustain. Energy Rev.* **2018**, *82*, 2880–2892. [[CrossRef](#)]
28. Sadeghi, A.; Hassanzadeh, H.; Harding, T.G. Thermal analysis of high frequency electromagnetic heating of lossy porous media. *Chem. Eng. Sci.* **2017**, *172*, 13–22. [[CrossRef](#)]
29. Mudgett, R.E. Electrical properties of foods. *Eng. Prop. Foods* **1986**, *2*, 389–455.
30. Horikoshi, S.; Schiffmann, R.F.; Fukushima, J.; Serpone, N. Microwave chemical and materials processing. In *Microwave Chemical and Materials Processing*; Springer: Singapore, 2018; pp. 33–45.
31. Eslamian, M. Excitation by acoustic vibration as an effective tool for improving the characteristics of the solution-processed coatings and thin films. *Prog. Org. Coat.* **2017**, *113*, 60–73. [[CrossRef](#)]
32. Mehdizadeh, M. *Microwave/RF Applicators and Probes: For Material Heating, Sensing, and Plasma Generation*; William Andrew: Norwich, NY, USA, 2015.
33. Wang, D.; Wang, X.; Jin, M.L.; He, P.; Zhang, S. Molecular level manipulation of charge density for solid-liquid TENG system by proton irradiation. *Nano Energy* **2022**, *103*, 107819. [[CrossRef](#)]
34. Huang, Z.; Luo, P.; Jia, S.; Zheng, H.; Lyu, Z. A sulfur-doped carbon-enhanced Na₃V₂(PO₄)₃ nanocomposite for sodium-ion storage. *J. Phys. Chem. Solids* **2022**, *167*, 110746. [[CrossRef](#)]
35. Li, S.; Wang, F.; Ouyang, L.; Chen, X.; Yang, Z.; Rozga, P.; Li, J.; Fofana, I. Differential Low-Temperature AC Breakdown between Synthetic Ester and Mineral Oils: Insights from both Molecular Dynamics and Quantum Mechanics. *IEEE Trans. Dielectr. Electr. Insul.* **2023**, *1*. [[CrossRef](#)]
36. Zhang, Y.; Jingshun, W.; Gao, H.; Chi, Q.; Zhang, T.-D.; Zhang, C.; Feng, Y.; Zhang, Y.; Cao, D.; Zhu, K. PEO/Li_{1.25}Al_{0.25}Zr_{1.75}(PO₄)₃ composite solid electrolytes for high-rate and ultra-stable all-solid-state lithium metal batteries with impregnated cathode modification. *Inorg. Chem. Front.* **2024**, *11*, 1289–1300. [[CrossRef](#)]
37. Guo, J.; He, B.; Han, Y.; Liu, H.; Han, J.; Ma, X.; Wang, J.; Gao, W.; Lü, W. Resurrected and Tunable Conductivity and Ferromagnetism in the Secondary Growth La_{0.7}Ca_{0.3}MnO₃ on Transferred SrTiO₃ Membranes. *Nano Lett.* **2024**, *24*, 1114–1121. [[CrossRef](#)] [[PubMed](#)]
38. Fu, Z.; Yang, B.; Shan, M.; Li, T.; Zhu, Z.; Ma, C.; Zhang, X.; Gou, G.; Wang, Z.; Gao, W. Hydrogen embrittlement behavior of SUS301L-MT stainless steel laser-arc hybrid welded joint localized zones. *Corros. Sci.* **2020**, *164*, 108337. [[CrossRef](#)]
39. Zhu, Q.; Chen, J.; Gou, G.; Chen, H.; Li, P. Ameliorated longitudinal critically refracted—Attenuation velocity method for welding residual stress measurement. *J. Mater. Process. Technol.* **2017**, *246*, 267–275. [[CrossRef](#)]
40. Wang, K.; Zhu, J.; Wang, H.; Yang, K.; Zhu, Y.; Qing, Y.; Ma, Z.; Gao, L.; Liu, Y.; Wei, S.; et al. Air plasma-sprayed high-entropy (Y_{0.2}Yb_{0.2}Lu_{0.2}Eu_{0.2}Er_{0.2})₃Al₅O₁₂ coating with high thermal protection performance. *J. Adv. Ceram.* **2022**, *11*, 1571–1582. [[CrossRef](#)]
41. Wu, Y.; Wu, H.; Zhao, Y.; Jiang, G.; Shi, J.; Guo, C.; Liu, P.; Jin, Z. Metastable structures with composition fluctuation in cuprate superconducting films grown by transient liquid-phase assisted ultra-fast heteroepitaxy. *Mater. Today Nano* **2023**, *24*, 100429. [[CrossRef](#)]
42. Wang, H.; Huang, Z.; Zeng, X.; Li, J.; Zhang, Y.; Hu, Q. Enhanced Anticarbonization and Electrical Performance of Epoxy Resin via Densified Spherical Boron Nitride Networks. *ACS Appl. Electron. Mater.* **2023**, *5*, 3726–3732. [[CrossRef](#)]
43. Huang, Z.; Zhang, Y.; Wang, H.; Li, J. Improved electrical resistivity-temperature characteristics of oriented hBN composites for inhibiting temperature-dependence DC surface breakdown. *Appl. Phys. Lett.* **2023**, *123*, 103501. [[CrossRef](#)]
44. Feng, X.; Sun, L.; Wang, W.; Zhao, Y.; Shi, J. Construction of CdS@ZnO core-shell nanorod arrays by atomic layer deposition for efficient photoelectrochemical H₂ evolution. *Sep. Purif. Technol.* **2023**, *324*, 124520. [[CrossRef](#)]
45. Yang, B.; Wang, H.; Zhang, M.; Jia, F.; Liu, Y.; Lu, Z. Mechanically strong, flexible, and flame-retardant Ti₃C₂T_x MXene-coated aramid paper with superior electromagnetic interference shielding and electrical heating performance. *Chem. Eng. J.* **2023**, *476*, 146834. [[CrossRef](#)]
46. Dong, Z.; Li, X.; Yamaguchi, H.; Yu, P. Magnetic field effect on the sedimentation process of two non-magnetic particles inside a ferrofluid. *J. Magn. Magn. Mater.* **2024**, *589*, 171501. [[CrossRef](#)]
47. Li, H.; Xu, X.; Liu, Y.; Hao, Y.; Xu, Z. Fluorophore molecule loaded in Tb-MOF for dual-channel fluorescence chemosensor for consecutive visual detection of bacterial spores and dichromate anion. *J. Alloys Compd.* **2023**, *944*, 169138. [[CrossRef](#)]
48. Guo, D.; Li, H.; Xu, Z.; Nie, Y. Development of pyrene-based MOFs probe for water content and investigations on their mechanochromism and acidochromism. *J. Alloys Compd.* **2023**, *968*, 172004. [[CrossRef](#)]
49. Lyu, J.; Huang, L.; Chen, L.; Zhu, Y.; Zhuang, S. Review on the terahertz metasensor: From featureless refractive index sensing to molecular identification. *Photonics Res.* **2024**, *12*, 194–217. [[CrossRef](#)]
50. Chen, D.; Wang, Q.; Li, Y.; Li, Y.; Zhou, H.; Fan, Y. A general linear free energy relationship for predicting partition coefficients of neutral organic compounds. *Chemosphere* **2020**, *247*, 125869. [[CrossRef](#)] [[PubMed](#)]

51. Ren, Z.; Zeng, H.; Zeng, X.; Chen, X.; Wang, X. Effect of Nanographite Conductive Concrete Mixed with Magnetite Sand Excited by Different Alkali Activators and Their Combinations on the Properties of Conductive Concrete. *Buildings* **2023**, *13*, 1630. [[CrossRef](#)]
52. Salmani, M.M.; Hashemian, M.; Khandan, A. Therapeutic effect of magnetic nanoparticles on calcium silicate bioceramic in alternating field for biomedical application. *Ceram. Int.* **2020**, *46*, 27299–27307. [[CrossRef](#)]
53. Khandan, A.; Ozada, N. Bredigite-Magnetite ($\text{Ca}_7\text{MgSi}_4\text{O}_{16}\text{-Fe}_3\text{O}_4$) nanoparticles: A study on their magnetic properties. *J. Alloys Compd.* **2017**, *726*, 729–736. [[CrossRef](#)]
54. Jasemi, A.; Moghadas, B.K.; Khandan, A.; Saber-Samandari, S. A porous calcium-zirconia scaffolds composed of magnetic nanoparticles for bone cancer treatment: Fabrication, characterization and FEM analysis. *Ceram. Int.* **2022**, *48*, 1314–1325. [[CrossRef](#)]
55. Shayan, A.; Abdellahi, M.; Shahmohammadian, F.; Jabbarzare, S.; Khandan, A.; Ghayour, H. Mechanochemically aided sintering process for the synthesis of barium ferrite: Effect of aluminum substitution on microstructure, magnetic properties and microwave absorption. *J. Alloys Compd.* **2017**, *708*, 538–546. [[CrossRef](#)]
56. Ghayour, H.; Abdellahi, M.; Nejad, M.G.; Khandan, A.; Saber-Samandari, S. Study of the effect of the Zn 2+ content on the anisotropy and specific absorption rate of the cobalt ferrite: The application of $\text{Co}_{1-x}\text{Zn}_x\text{Fe}_2\text{O}_4$ ferrite for magnetic hyperthermia. *J. Aust. Ceram. Soc.* **2018**, *54*, 223–230. [[CrossRef](#)]
57. Rodriguez-Vargas, B.R.; Stornelli, G.; Folgarait, P.; Ridolfi, M.R.; Miranda Pérez, A.F.; Di Schino, A. Recent advances in additive manufacturing of soft magnetic materials: A review. *Materials* **2023**, *16*, 5610. [[CrossRef](#)] [[PubMed](#)]
58. Pošković, E.; Franchini, F.; Ferraris, L.; Fracchia, E.; Bidulska, J.; Carosio, F.; Bidulsky, R.; Grande, M.A. Recent advances in multi-functional coatings for soft magnetic composites. *Materials* **2021**, *14*, 6844. [[CrossRef](#)] [[PubMed](#)]
59. Bullivant, J.P.; Zhao, S.; Willenberg, B.J.; Kozissnik, B.; Batich, C.D.; Dobson, J. Materials characterization of Feraheme/ferumoxytol and preliminary evaluation of its potential for magnetic fluid hyperthermia. *Int. J. Mol. Sci.* **2013**, *14*, 17501–17510. [[CrossRef](#)] [[PubMed](#)]
60. Szweczyk, R. Validation of the anhysteretic magnetization model for soft magnetic materials with perpendicular anisotropy. *Materials* **2014**, *7*, 5109–5116. [[CrossRef](#)]
61. Harja, M.; Buema, G.; Lupu, N.; Chiriac, H.; Herea, D.D.; Ciobanu, G. Fly ash coated with magnetic materials: Improved adsorbent for Cu (II) removal from wastewater. *Materials* **2020**, *14*, 63. [[CrossRef](#)]
62. Ajinkya, N.; Yu, X.; Kaithal, P.; Luo, H.; Somani, P.; Ramakrishna, S. Magnetic iron oxide nanoparticle (IONP) synthesis to applications: Present and future. *Materials* **2020**, *13*, 4644. [[CrossRef](#)]

Disclaimer/Publisher's Note: The statements, opinions and data contained in all publications are solely those of the individual author(s) and contributor(s) and not of MDPI and/or the editor(s). MDPI and/or the editor(s) disclaim responsibility for any injury to people or property resulting from any ideas, methods, instructions or products referred to in the content.